Astronomy & Astrophysics manuscript no. ELG_observation
September 18, 2015

The SDSS-IV eBOSS emission-line galaxy pilot survey

J. Comparat,[1,2,⋆,⋆⋆], T. Delubac[3], S. Jouvel[4], A. Raichoor[5], J-P. Kneib[3,6], C. Yèche[5], F. B. Abdalla[4,7], C. Le Cras[8], C. Maraston[8], D. M. Wilkinson[8], G. Zhu[9], E. Jullo[6], F. Prada[1,2,10], D. Schlegel[11], Z. Xu[12], H. Zou[12], J. Bautista[13], D. Bizyaev[14,15], A. Bolton[13], J. R. Brownstein[13], K. S. Dawson[13], S. Escoffier[16], P. Gaulme[14], K. Kinemuchi[14], E. Malanushenko[14], V. Malanushenko[14], V. Mariappan[13], J. A. Newman[17], D. Oravetz[14], K. Pan[14], W. J. Percival[8], A. Prakash[17], D. P. Schneider[18,19], A. Simmons[14], T. M. C. Abbott[20] S. Allam[21], M. Banerji[22,23], A. Benoit-Lévy[4], E. Bertin[24,25], D. Brooks[4], D. Capozzi[8], A. Carnero Rosell[26,27], M. Carrasco Kind[28,29], J. Carretero[30,31], F. J. Castander[31], C. E. Cunha[32], L. N. da Costa[26,27], S. Desai[33,34], P. Doel[4], T. F. Eifler[35,36], J. Estrada[21], B. Flaugher[21], P. Fosalba[30], J. Frieman[21,37], E. Gaztanaga[30], D. W. Gerdes[38], D. Gruen[39,40], R. A. Gruendl[28,29], G. Gutierrez[21], K. Honscheid[41,42], D. J. James[20], K. Kuehn[43], N. Kuropatkin[21], O. Lahav[4], M. Lima[44,26], M. A. G. Maia[26,27], M. March[35], J. L. Marshall[45], R. Miquel[46,31], A. A. Plazas[36], K. Reil[47], N. Roe[11], A. K. Romer[48], A. Roodman[32,47], E. S. Rykoff[32,47], M. Sako[35], E. Sanchez[49], V. Scarpine[21], I. Sevilla-Noarbe[49,28], M. Soares-Santos[21], F. Sobreira[21,26], E. Suchyta[41,42], M. E. C. Swanson[29], G. Tarle[38], J. Thaler[50], D. Thomas[8], A. R. Walker[20], and Y. Zhang[38]

(Affiliations can be found after the references)

September 18, 2015

ABSTRACT

The Sloan Digital Sky Survey IV extended Baryonic Oscillation Spectroscopic Survey (SDSS-IV/eBOSS) will observe approximately 270,000 emission-line galaxies (ELGs) to measure the Baryonic Acoustic Oscillation standard ruler (BAO) at redshift 0.9. To test different ELG selection algorithms, based on data from several imaging surveys, 9,000 spectra were observed with the SDSS spectrograph as a pilot survey. First, we provide a detailed description of each target selection algorithm tested. Then, using visual inspection and redshift quality flags, we find that the automated spectroscopic redshifts assigned by the pipeline meet the quality requirements for a robust BAO measurement. Also, we show the correlations between sky emission, signal-to-noise ratio in the emission lines and redshift error. As a result, we provide robust redshift distributions for the different target selection schemes tested. Finally, we infer two optimal target selection algorithms to be applied on DECam photometry that fulfill the eBOSS survey efficiency requirements.

Key words. cosmology - survey - spectroscopy - galaxy - emission lines

1. Introduction

Galaxy surveys permit the study of the cosmological structures formed by the network of galaxies as well as the study of the evolution of galaxies. The recent increase of the number of multiplexing of spectrographs (Le Fèvre et al. 2003; Sharp et al. 2006; Smee et al. 2013; Flaugher & Bebek 2014) and of the field of view of photometric cameras (Gunn et al. 1998; Boulade et al. 2003; Flaugher et al. 2015) allow galaxy surveys to cover larger areas of the sky and measure large numbers of accurate redshifts. The precision of a cosmological statement based on a galaxy survey is directly related to the volume sampled by the survey: the larger, the better. To extract cosmological information from a magnitude-limited galaxy survey one thus constructs the largest possible volume-limited sample (Martinez & Saar 2002). To enhance the volume covered and increase survey efficiency, galaxy surveys push the high-redshift limit the furthest possible and they pre-select galaxies, by discarding low-redshift faint galaxies, to obtain an observed sample as close as possible to the desired volume-limited sample.

Three recent surveys successfully applied a color selection to a magnitude-limited sample to map more efficiently a given redshift range and extract cosmological information. The Baryonic Oscillation Spectroscopic Survey (BOSS: Dawson et al. 2013; Eisenstein et al. 2011) observed a specific part of the galaxy population, the most massive ellipticals at redshift 0.57, by selecting in the color-color diagram $g - r$, $r - i$ (Maraston et al. 2013). BOSS is the first to measure at the percent level the Baryonic Acoustic Oscillation standard ruler (BAO: Seo & Eisenstein 2003) that constrains directly the cosmological model (Anderson et al. 2014). The WiggleZ survey targeted star-forming galaxies at redshift 0.6 (Drinkwater et al. 2010) and measured the BAO standard ruler at

⋆ j.comparat@csic.es
⋆⋆ Severo Ochoa IFT Fellow

the 5 % level (Kazin et al. 2014). Finally, the VIMOS Public Extragalactic Redshift Survey (VIPERS, Guzzo et al. 2014) observed galaxies at redshift 0.8 (Guzzo et al. 2014) and measured the growth rate of structure at the 17% level (de la Torre et al. 2013). The measurements of standard rulers and of the growth rate of structure are key to understand the cosmological model (Weinberg et al. 2013) but they do not require the galaxy sample to be volume limited. In fact, as demonstrated by the measurement of the BAO feature in the Lyα forest of quasars (Delubac et al. 2015), the BAO feature is an intrinsic property of the matter field and does not require a volume-limited sample. Therefore, one can observe spectroscopically any tracer of the matter field, provided its density is sufficient to overcome the shot noise and that an accurate redshift can be obtained in a short time, so that a large ($> h^{-3}\mathrm{Gpc}^3$) volume can be covered within a few years of observations.

The extended baryonic oscillation spectroscopic survey (eBOSS, Dawson et al. 2015) uses color selection to identify three types of galaxies: luminous red galaxies (LRGs, Prakash et al. 2015), emission-line galaxies (ELGs, this paper) and quasars (QSOs, Myers et al. 2015). The ELG and QSO samples will not provide volume-limited samples. eBOSS will measure the BAO distance ladder to the 1% precision at redshift 0.7 using LRGs , 2% at redshift 0.9 using ELGs, 1% at redshift 1.5 using QSOs and 1% at redshift 2.3 using the Lyα forest (Zhao G. et al. in prep.).

For both ELGs and QSOs, schemes that select targets for spectroscopy exist using either color selection (Comparat et al. 2013b; Schneider et al. 2010) or higher dimensional algorithms (Raichoor et al. 2015; Bovy et al. 2012).

The target selection of the ELG for BAO surveys is driven by the requirement to acquire as many spectra as possible in the smallest amount of observing time in order to maximize the volume covered by the survey. In addition, SDSS-IV eBOSS faces another challenge: to develop the best targeting algorithm implementable with existing photometry to construct a homogeneous galaxy sample around redshift 0.9. To assess algorithms, eBOSS tested them on a 10 deg^2 sky patch covered by many photometric surveys around $\alpha \sim 36°$ and $\delta \sim -4.5°$. This region was indeed observed by the following surveys SDSS, CFHT-LS Wide, DES, SCUSS and WISE (Ahn et al. 2012; Gwyn 2012; Banerji et al. 2015; Zou et al. 2015; Wright et al. 2010, respectively).

In this paper, we analyze the pilot survey observations from eBOSS ELG carried at the SDSS telescope (Gunn et al. 2006). We describe in section 2 the available photometry for targeting, the selection algorithms applied and the corresponding galaxy population observed. Section 3 describes how precisely redshifts are measured automatically. In section 4, we propose two selection schemes that are suited for the eBOSS ELG observations. The difficulty to find a deep and homogeneous photometric sample to target from and that covers a large fraction of the sky visible by the SDSS telescope is discussed in two companion papers: Jouvel et al. (2015) and Delubac et al. (2015).

Throughout the paper, we quote magnitudes in the AB system (Oke & Gunn 1983) and we provide the measurements in a flat ΛCDM cosmology $h = 0.7$, $\Omega_m = 0.3$.

2. Data

The SDSS-BOSS spectrograph is an optical multi-fiber spectrograph mounted on the 2.5 m f/5 modified Ritchey-Chretien altitude-azimuth telescope located at the Apache Point Observatory, (APO Gunn et al. 2006; Smee et al. 2013). SDSS spectra cover the wavelength range $3,600 < \lambda < 10,400$Å at an average resolution of 2000. The wavelength λ is calibrated to vacuum wavelengths. The BOSS spectrophotometric calibration is accurate at the <5% level in the r-band and <10% in the other bands (Shen et al. 2015).At the APO facility, 9000 fibers, or ten plates, were dedicated to the eBOSS ELG pilot survey. The exposure time is 4×15 minutes for each plate. The test extends over ∼10 deg^2 and is located around α(J2000)∼ 36° and δ(J2000)∼ −4.5°. They are labeled under the 'chunks' – SDSS jargon for an observational run – 'eboss6' (plates number 8123 to 8130) and 'eboss7' (plates number 8355 and 8356). The spectra are reduced with the current SDSS pipeline (Bolton et al. 2012). They have strong emission lines and weak absorption lines; see Fig 1. These clear features enable clean redshift identification for about 75% of the targets. The position of the observed targets on the sky and the measured line flux as a function of redshift for the main emission lines [OII] , Hβ and [OIII] are presented in Fig. 2. Most lines have a flux greater than log(flux / erg $\cdot$ s^{-1} $\cdot$ cm^{-2})> −16.5. The position of the observation on the sky, coded by the level of Galactic extinction (Schlegel et al. 1998), shows that we observed a region with low extinction. The last panel shows the redshift distribution of the different algorithms observed. Finally, Table 1 shows side by side all the selections and their efficiency at targeting ELGs.

Table 1. Summary of the selections tested ordered by median redshift. The efficiency is the number density of galaxies identified in the redshift range specified divided by the total number density of galaxies. The columns 'photometry' informs what combination of photometry was used, 1: SCUSS + SDSS; 2: SCUSS + SDSS + WISE, 3: SDSS + WISE; 4: DECam. The uncertainties on the number densities and efficiencies are comprised between 1.5 and 3 percent but for the sake of readability, we reported all uncertainties in the Tables in appendix.

selection name	photometry	magnitude selection upper bound	density [deg^{-2}]	median redshift	ID rate	efficiency $0.6 < z < 1$	efficiency $0.7 < z < 1.1$
gri-Uri	1	$g < 22.5$ or $U < 22.5$	197	0.734	0.68	0.52	0.40
griW	2	$g < 22.5$	196	0.767	0.72	0.56	0.42
UgrizW bright all	3	$g < 22.5$	196	0.778	0.78	0.59	0.49
UgrizW	3	$g < 22.7$	199	0.788	0.76	0.59	0.52
des bright	4	$g < 22.8$	615	0.843	0.76	0.53	0.53
decam 190	4	$g < 22.8$	190	0.855	0.91	0.74	0.78
decam 240	4	$g < 22.8$	240	0.871	0.90	0.69	0.74
des faint	4	$r < 22.8$	650	0.901	0.71	0.41	0.47

We created a matched detection catalog from the SDSS, CFHT-LS Wide, DES, SCUSS and WISE photometric surveys and drew ELG targets for spectroscopic observations using the following schemes. We study two scenarios, one based on the combined SDSS, SCUSS, WISE photometry and one based on DECam photometry.

2.1. ELG selection with SCUSS - SDSS - WISE

Using the forced-photometry technique on the SDSS r-band detected objects (75% complete at 22.5) on the SCUSS and WISE data (Lang et al. 2014; Zou et al. 2015), we created a multi-band catalog of detections. This catalog extends on the full South Galactic Cap; see Raichoor et al. (2015) and Delubac et al. (2015) for the complete description of the catalog.

The density required to measure the BAO standard ruler in the two-point correlation function of ELGs covering the redshift range $0.6 < z < 1.0$ (mean 0.8) is 180 targets per deg^{-2} (Comparat et al. 2013b). We tested two approaches, a color selection and a Fisher's linear discriminant (Fisher 1936) selection, attempting to maximize both the share of ELGs in the redshift range $0.6 < z < 1.0$ and the mean redshift of the sample.

2.1.1. Color selection

The color selection uses two color spaces $U - r - i$ and $g - r - i$ (see Fukugita et al. 1996, that defines the filters). We call this selection the "gri-Uri" selection. This is a further optimization of the color selections observed in Comparat et al. (2013b) for the needs of eBOSS. It selects a mean of 197 targets per deg^2 (averaged over ∼50 deg^2) by applying the following selections on the photometric catalog.

1. RESOLVE_STATUS in the SDSS photometry has SURVEY_PRIMARY on
2. $g_{\rm model}, r_{\rm model}, i_{\rm model} > 0$ and $g^{\rm err}_{\rm model} < 0.6$ and $r^{\rm err}_{\rm model} < 1$ and $i^{\rm err}_{\rm model} < 0.4$
3. and (a) OR (b) with:
   (a) $21 \leq g_{\rm model} < 22.5$ and $r_{\rm model} < 22.5$ and $i_{\rm model} < 21.6$ and $g_{\rm model} - r_{\rm model} < 0.8$ and $r_{\rm model} - i_{\rm model} > 0.8$
   (b) $20 < g_{\rm model} < 23$ and $r_{\rm model} < 22.5$ and $i_{\rm model} < 21.6$ and $21 < U_{\rm modelAdd} < 22.5$ and $r_{\rm model} - i_{\rm model} > 0.7$ and $r_{\rm model} - U_{\rm modelAdd} > 0.7 - 3.5 * (r_{\rm model} - i_{\rm model})$

where magnitudes are dust extinction corrected using the coefficients from Schlegel et al. (1998). $mag_{\rm model}$ are from the model magnitudes from SDSS DR12 (Alam et al. 2015), $U_{\rm modelAdd}$ is the U-band model magnitude from SCUSS. Given the uncertainty on the magnitude at the depth of the selection ($g < 22.5$ and $U < 22.5$), all coefficients in the selection were rounded to the first decimal without impacting the properties of the galaxy population selected. A total of 2,484 targets were observed in a 13.36 deg^2 region, which corresponds to a Target Sampling Rate TSR=$N_{observed}/N_{targeted}$= 94.4%. The TSR does not depend on magnitude nor on redshift and the observations have enough overlap so that fiber collision is negligible. The observed sample is thus a fair sample of the complete sample. In the Tables A.1, A.2, A.3 where redshift distributions are reported, we give an estimate of the uncertainty on the number density by approximating the distribution per bin to follow a Poisson distribution, i.e. that the uncertainty on N is $\sigma_N = N\sqrt{N_{obs}}/N_{obs}$. We securely measured the redshifts of 68±2% of the targets as galaxies or quasars; see Table A.1. This sample has a mean redshift of 0.734. The percentage of detections classified as stars is 7.7%, which leaves a 25% fraction of unknown objects.

2.1.2. Fisher selection

The Fisher selection algorithm allows us to make further-optimized color-selections in a greater number of dimensions which slightly improves the selection efficiency. For a thorough description of the Fisher selection method, see Raichoor et al. (2015). We constituted a training spectroscopic data sample using the SDSS, BOSS ELG, VIPERS, DEEP2, zCOSMOS and VVDS surveys (Alam et al. 2015; Comparat et al. 2015; Guzzo et al. 2014; Newman et al. 2013; Lilly et al. 2009; Le Fèvre et al. 2013, respectively) to derive the best possible selection with a Fisher discriminant. We tested it in the chunk eboss7, that is a sub-region of the eboss6 chunk. We considered two types of selection, first using the combination of SDSS and WISE, designated 'griW', and secondly using the combination of SCUSS, SDSS and WISE, named 'UgrizW'.

We emphasize that the selections published in Raichoor et al. (2015) are slightly different from those tested with eboss7, due to further optimization of the selection function based on the eboss6-7 spectroscopic information.

We use the first two filters of the WISE photometry W1 and W2 to construct a composite extinction-corrected AB magnitude, $W_{\rm model}$, which takes advantage of both measurements (see Myers et al. 2015 for the details about the WISE composite magnitude). First, we convert W1 and W2 magnitudes to the AB magnitude system (AB = Vega + dm, with dm(W1)=2.699 and dm(W2)=3.339). We then define W as follows:

1. W = W1, if no W2 measurement
2. W= W2, if no W1 measurement
3. else: flux(W) = (flux(W1) + 0.5*flux(W2))/1.5, if both W1 and W2 measurements are present.

For the uncertainty, we construct $W^{\rm err}_{\rm model}$ from W1_MAGERR and W2_MAGERR using the propagation of uncertainties in quadrature. For the extinction, we consider: extinction_W = extinction_W1, because abs(extinction_W1-extinction_W2)<5e-3 in the test region). Finally, we use $W_{\rm model} = W - extinction\_W1$.

Fisher UgrizW:

The Fisher 'UgrizW' selection selection was adopted as a first priority and contains:

1. RESOLVE_STATUS in the SDSS photometry has SURVEY_PRIMARY on
2. OBJC_TYPE=3 or $r_{\rm model}$ >22
3. 20.0< $g_{\rm model}$ <22.7 and $g^{\rm err}_{\rm model}$ <0.5 and 19.0< $r_{\rm model}$ <22.5 and $r^{\rm err}_{\rm model}$ <0.5 and 19.0< $i_{\rm model}$ <21.5 and $i^{\rm err}_{\rm model}$ <0.5 and 17.0< $W_{\rm model}$ <21.0 and $W^{\rm err}_{\rm model}$ <0.5 and $U_{\rm modelAdd} > 0$
4. 1.23<Fisher$_{\rm UgrizW}$ <5.0

with Fisher$_{\rm UgrizW}$ = $-0.390197(u_{\rm modelAdd} - r_{\rm model}) - 0.497885(g_{\rm model} - r_{\rm model}) + 0.0734933(r_{\rm model} - i_{\rm model}) + 0.480957(r_{\rm model} - W_{\rm model}) + 0.152151(r_{\rm model} - z_{\rm model}) + 0.847598$. It has a target density of 199 per square degree. A total of 76% are identified as galaxies or QSOs with a mean redshift at 0.788. The detections classified as stars are 1.7%, and 22% remain unknown.

Fisher UgrizW bright:

The Fisher selection UgrizW bright selection was chosen as a second priority; the overlap with the first selection is broad.

1. same as the Fisher UgrizW selection points 1 to 3 (not 4)
2. $g_{\rm model}$ <22.5 and 1.13<Fisher$_{\rm UgrizW}$ <1.23

It has a target density of 43 per square degree; 71% are identified as galaxies or QSOs with a mean redshift at 0.724. The detections classified as stars are 0.34%, and 28% remain unknown. It seems less efficient, but the uncertainty on the efficiency is of 9% due to the low number of targets.

Fisher UgrizW bright all:

The Fisher selection 'UgrizW bright all' is the same as the UgrizW bright, but without the FisherUgrizW<1.23 selection. It has a target density of 196 per square degree; 78% are identified as galaxies or QSOs with a mean redshift at 0.778. The detections classified as stars are 1.47%, and 20% remain unknown.

Fisher griW:

The Fisher selection griW was selected as a third priority and does not use the SCUSS U band nor the SDSS z band that are quite shallow.

1. RESOLVE_STATUS in the SDSS photometry has SURVEY_PRIMARY on
2. OBJC_TYPE=3 or $r_{\rm model}$ >22
3. 20.0< $g_{\rm model}$ <22.5 and $g^{\rm err}_{\rm model}$ <0.5 and 19.0< $r_{\rm model}$ <22.5 and $r^{\rm err}_{\rm model}$ <0.5 and 19.0< $i_{\rm model}$ <21.5 and $i^{\rm err}_{\rm model}$ <0.5 and 17.0< $W_{\rm model}$ <21.0 and $W^{\rm err}_{\rm model}$ <0.5
4. 0.61<Fisher$_{\rm griW}$ <5.00

with Fisher$_{\rm griW}$ = $-0.50972(g_{\rm model} - r_{\rm model}) + 0.304366(r_{\rm model} - i_{\rm model}) + 0.353073(r_{\rm model} - W_{\rm model}) + 0.0306172$. This selection has a target density of 196 per square degree; 72% are identified as galaxies or QSOs with a mean redshift at 0.788. The detections classified as stars are 2.61%, and 25% remain unknown.

About the Fisher selections

The priority scheme did not influence the completeness from one sample relative to another and the observed samples are fair subsamples of the complete selection. The target sampling rate for the first priority algorithm is 96.55% and for the third it is 93.81%.

For the same target density, the Fisher selections improve the identification rate up to 10%, increase the mean redshift and diminish the contamination by lower redshift galaxies and stars. The first decile of the redshift distribution is above 0.6 compared to 0.43 for the gri-Uri selection, see Table 3. Table A.2 gives the detailed density of galaxies observed as a function of redshift using the Fisher approach.

2.2. ELG selection with DECam - DES photometry

The Dark Energy Camera (DECam Flaugher et al. 2015) was mounted, installed and commissioned in 2012 on the Blanco 4-meter telescope at Cerro Tololo Inter-American Observatory, in Chile (Doel et al. 2012).

The Dark Energy Survey (DES) is an imaging survey of the grizY photometric bands (Flaugher & DES Collaboration 2013; Diehl et al. 2014) that will cover 5000 deg^2 to an unprecedented 5σ depth of $i_{AB} < 24$ (Flaugher 2012) using DECam. A Science Verification (SV) period followed of data acquisition between end of 2012 through February 2013. As the data were taken shortly after DECam commissioning and were used to test survey operations and assess data quality, the DES-SV data quality isn't as good as the full survey data is expected to be, but it was deep enough for our purpose. The SV fields were chosen to cover sky areas

observed by spectroscopic galaxy surveys such as DEEP2 (Newman et al. 2013), VVDS (Le Fèvre et al. 2013). To test the target selections, we used the DES-SV around the CFHTLS-W1 field.

This photometry is about ten times deeper than the SDSS photometry and therefore allows a narrower and more efficient redshift selection; see the discussion from Comparat et al. (2013b). For instance, the scatter in the magnitude-color or color-color diagrams being smaller, it permits cleaner selections. Given that the area available to target from DECam-based imaging is smaller, we tried denser selections that extend to higher redshifts.

We performed two tests selecting either brighter and redder galaxies (DES bright) or fainter and bluer galaxies (DES faint). These objects are targeted as last priority objects after the gri-Uri targets in eboss6 and after the Fisher targets in eboss7.

DES, bright selection

The 'bright selection' is defined by

1. $20.5 < g_{\rm model} < 22.8$
2. and -0.7 $< g_{\rm model} - r_{\rm model} < 0.9$ and $0 < r_{\rm model} - z_{\rm model} < 2$ and $r_{\rm model} - z_{\rm model} > 0.4 * (g_{\rm model} - r_{\rm model}) + 0.4$
3. $g_{2"} - g_{\rm model} < 2$ and $r_{2"} - r_{\rm model} < 2$ and $z_{2"} - z_{\rm model} < 2$: it rejects fake detections near bright stars or saturated bright stars.

where $mag_{\rm model}$ is the model magnitude (MAG_DETMODEL) and $mag_{2"}$ is the 2" diameter aperture magnitude (MAG_APER_4) reported by the DES pipeline. We designate this selection by 'des bright'. It has a target density of 615 per square degree; 76% are identified as galaxies with a mean redshift at 0.843. The detections classified as stars are 7.7%, and 16% remain unknown.

DES, faint selection

The 'faint selection' is defined by

1. $g_{\rm model} > 20.45$ and $r_{\rm model} < 22.79$
2. $0.285 < r_{\rm model} - z_{\rm model} < 1.585$ and $g_{\rm model} - r_{\rm model} < 1.1458\,(r_{\rm model} - z_{\rm model}) - 0.209$ and $g_{\rm model} - r_{\rm model} < 1.4551 - 1.1458\,(r_{\rm model} - z_{\rm model})$
3. $g_{2"} - g_{\rm model} < 2$ and $r_{2"} - r_{\rm model} < 2$ and $z_{2"} - z_{\rm model} < 2$

It has a target density of 650 per square degree. 71% are identified as galaxies with a mean redshift at 0.9. The detections classified as stars are 6.3% and 23% remain unknown. The observed redshift distribution is given in Table A.3. We designate this selection by 'des faint'.

About the DES-based selections

The DES-based selections were observed at a lower completeness level (60%-70%) and the average redshift is higher than the one of the SDSS-based selections.

2.3. Pilot observations, summary

We compare the target density and redshift distribution of the different selection algorithms and data sets in Tables 2 and 3. It is difficult to target ELGs beyond redshift one using the combination of the SCUSS - SDSS and WISE photometry; however, it is feasible with the DES photometry.

Using shallower photometry, to reach the density of galaxies required by eBOSS, we are forced to target near the 5σ limit of the photometry. In this regime, the Malmquist bias becomes non-negligible and the actual mean magnitude of the selection is fainter than the magnitude selection imposed on the data, so that the sample becomes dominated by fainter galaxies and the redshift identification rate decreases.

2.4. Previous ELG observations with SDSS spectrograph

During the SDSS-III BOSS survey, 11,883 ELG were observed and visually inspected (see Comparat et al. 2013b, 2015; Alam et al. 2015). We add this sample to the eBOSS pilot survey to study the reliability of automated redshift assignment. The plates that contain ELGs are 4386-4389, 4391, 4392, 4394, 4395, 4397, 4399 with a sparse ELG sampling and 5017, 5018, 6931-6933, 7239-7243, 7245-7247 that are dedicated plates.

2.5. VIPERS data, a parent sample

To understand the completeness properties of the ELG selection function, we use VIPERS that has a > 90% redshift determination rate for magnitudes brighter than $i < 22.5$ and at redshift larger than $z > 0.6$. We use its first data release, containing 57,204 slit-extracted 1d-spectra and their measured and visually-inspected redshifts (Garilli et al. 2014), from 45-minute long exposures. The VIPERS data covers the fields W1 and W4 of the CFHT-LS. There is a small overlap between the eBOSS ELG footprint and the VIPERS W1 field.

Table 2. eBOSS ELG surface densities (after applying the bright star mask). For each selection scheme the first line gives the result of the eboss6 chunk and the second line the combination of eboss6 and eboss7 chunks. Note that the areal extent of eboss7 is contained in eboss6.

selection	Targeted			Observed			fraction
name	N	area	density	N	area	density	observed
		[deg^2]	[deg^{-2}]		[deg^2]	[deg^{-2}]	[%]
gri-Uri	9686	49.18	196.94	2484	13.36	185.90	94.39
-	-	-	-	1588	8.82	180.11	91.45
Fisher griW	9639	49.18	195.99	1375	13.36	102.90	52.50
-	-	-	-	1621	8.82	183.85	93.81
Fisher UgrizW bright	2143	49.18	43.57	188	13.36	14.07	32.29
-	-	-	-	303	8.82	34.37	78.87
Fisher UgrizW bright all	9676	49.18	196.74	1287	13.36	96.32	48.96
-	-	-	-	1595	8.82	180.90	91.95
Fisher UgrizW	9798	49.18	199.22	1204	13.36	90.10	45.23
-	-	-	-	1696	8.82	192.36	96.55
des bright	8306	13.50	615.26	3272	9.20	355.65	57.81
-	-	-	-	3842	8.82	435.75	70.82
des faint	8776	13.50	650.07	3249	9.20	353.15	54.32
-	-	-	-	3406	8.82	386.30	59.42

Table 3. Moments of the eBOSS ELG redshift distribution: first decile D10, first, second (median) and third quartiles Q25, Q50, Q75 and last decile D90.

selection	D10	Q25	Q50	Q75	D90
gri-Uri	0.432	0.633	0.734	0.820	0.904
griW	0.604	0.690	0.767	0.852	0.945
UgrizW bright	0.600	0.661	0.724	0.814	0.928
UgrizW bright all	0.628	0.710	0.778	0.862	0.956
UgrizW	0.639	0.723	0.788	0.866	0.958
des bright	0.619	0.745	0.843	0.964	1.198
des faint	0.729	0.801	0.901	1.119	1.441

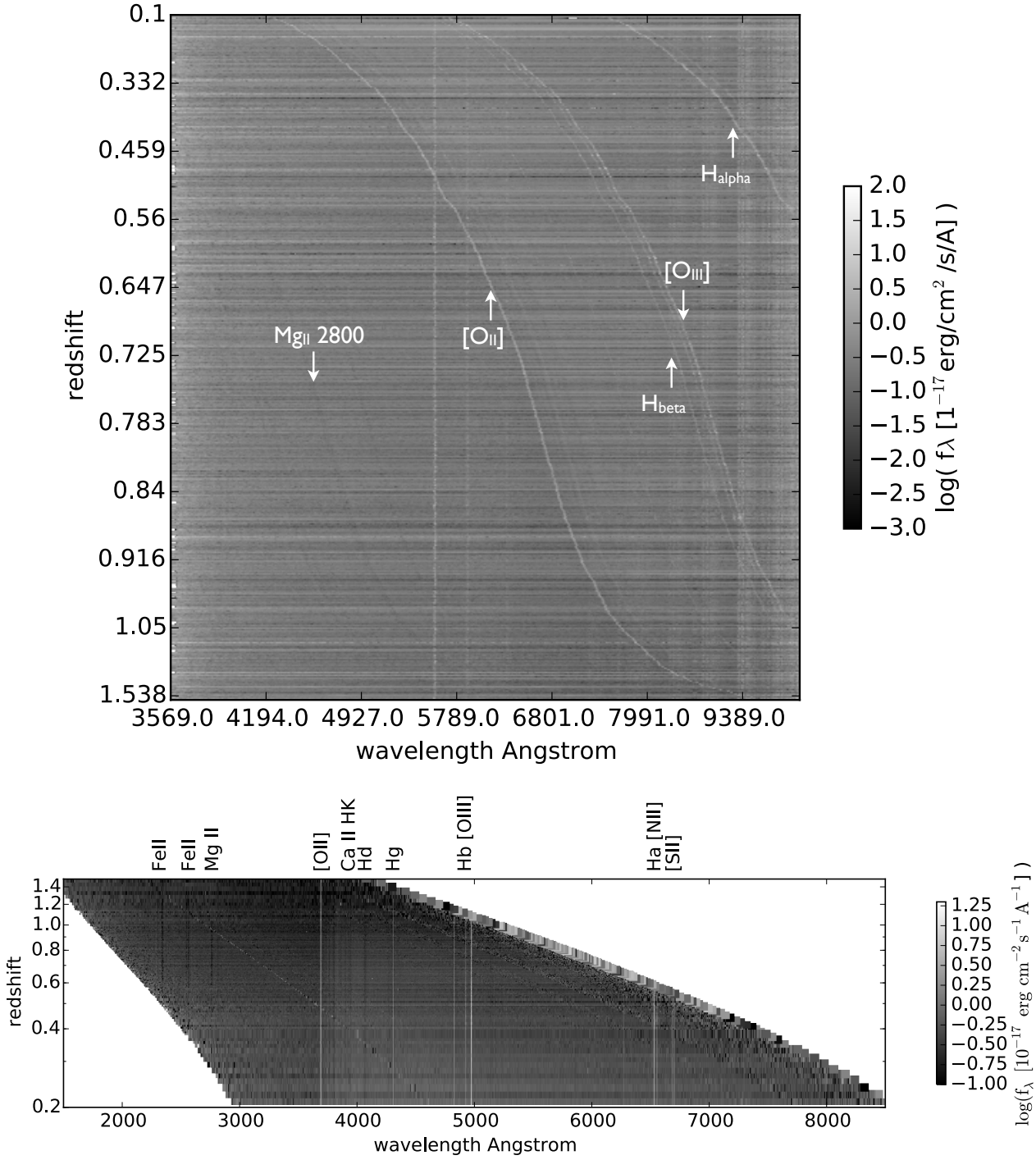

Fig. 1. Top panel. ELG spectra observed sorted by redshift. Each horizontal line corresponds to one spectrum. Vertical patterns correspond to the residuals of the sky subtraction. Diagonal patterns are the emission and absorption lines seen in the galaxy spectra. As redshift increases, we see the [OII] , Hβ , [OIII] ,Hα emission lines being redshifted. Starting at redshift 0.5, UV absorption lines enter the spectrograph window. **Bottom panel** ELG spectra stacked by 50, ordered as a function of redshift represented in the rest-frame. The spectral features align vertically and are detected with higher signal-to-noise-ratio, in particular the absorption lines in the UV. Extended details about the UV absorption and emission systems are given in Ben Zhu et al. (2015).

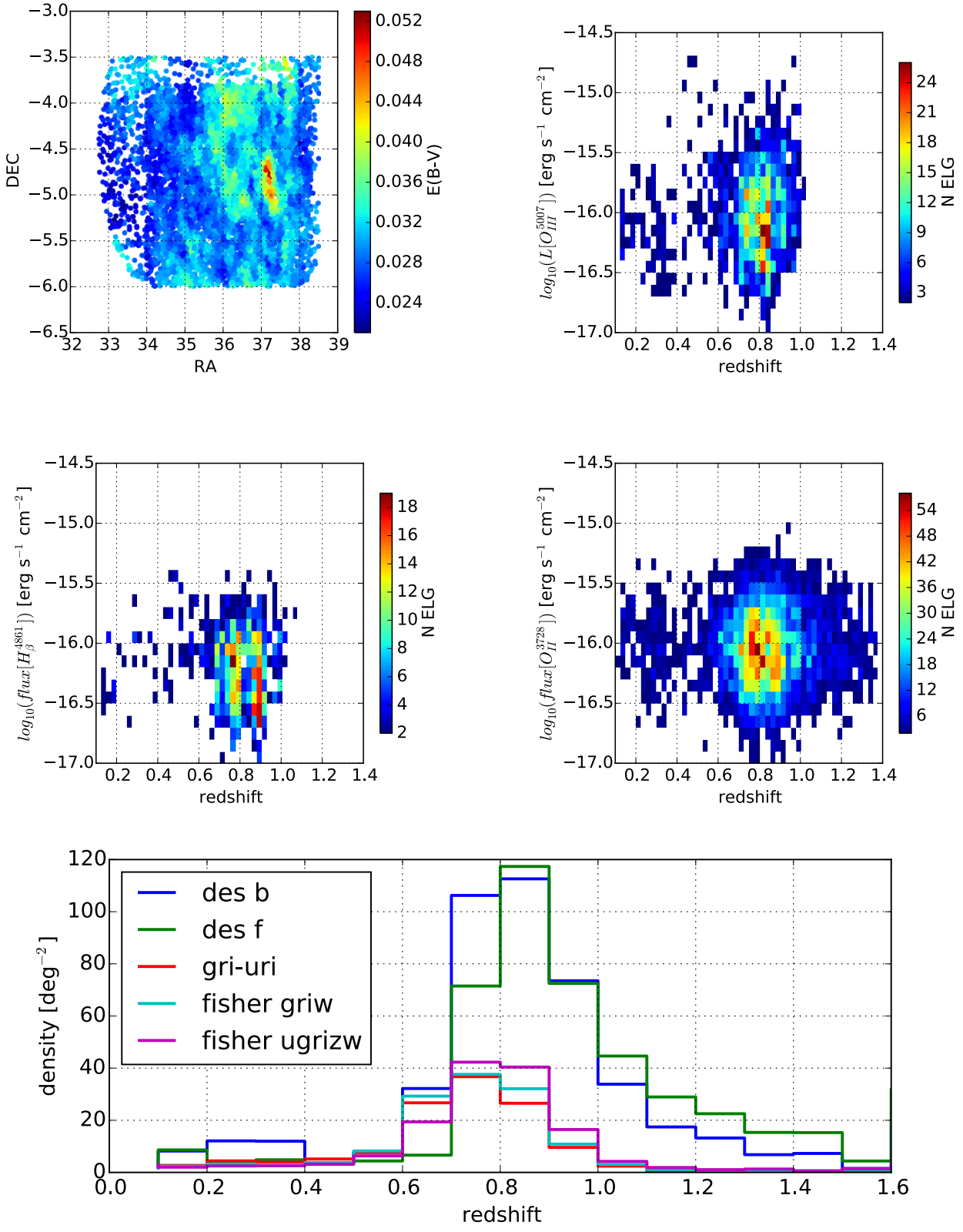

Fig. 2. Summary of eBOSS ELG pilot observations. RA vs. DEC colored with Galactic extinction (top left). The area covered has a low Galactic extinction. Number of ELGs as a function of redshift and line flux for the three features ([OIII] , Hβ , and [OII]) measured with a signal-to-noise ratio larger than 5. [OII] is the strongest emission line and is seen throughout the redshift range. The bottom panel shows the redshift distribution obtained for each selection tested. The DES-based selections have a higher density and a higher mean redshift.

3. Redshift determination

The SDSS/BOSS pipeline (Bolton et al. 2012) provides reliable redshifts for most of the ELGs observed. To measure the two-point correlation function in redshift space for BAO in the redshift range 0.6 to 1.1, we require a redshift precision better than 300 km s^{-1} and the share of redshifts with an error larger than 1000 km s^{-1} (so-called 'catastrophic' redshifts) to be smaller than 1%. In this section, we investigate the precision obtained on the estimation of the redshifts and the rate of catastrophic errors. In total, we visually inspected 13,450 of the 21,500 spectra reduced by the same pipeline to assess the plausibility of the redshift assignment. We have not inspected all of them, as it is a highly time-consuming task.

3.1. Redshift assigned, flags, reliability

The reliability of the redshift of an emission-line galaxy is mainly correlated with the signal-to-noise ratio (SNR) of the detection of the line(s) defined by

$$\mathrm{SNR_{line}} = \text{fitted flux}_{\mathrm{line}} \,/\, \text{error fitted flux}_{\mathrm{line}}. \quad (1)$$

In some cases, it can be correlated to the detection of a small 4000 Å break. To compare the visual inspection redshifts with the pipeline values, we classify the spectra according to the strength of their emission lines, using a flag 'zQ', and to the features seen in the continuum, using a flag 'zCont'. We define the flags in Table 4. In this classification, we consider a line with $3 \leq SNR < 5$ as a low SNR detection and a line with $SNR \geq 5$ as a high SNR detection. To give an order of magnitude, the SNR value in the fitted line flux correspond roughly to the SNR value in the pixel that contains the maximum of the line. This classification follows conventions used by spectroscopic surveys such as VVDS, DEEP2 or zCOSMOS (Le Fèvre et al. 2013; Newman et al. 2013; Lilly et al. 2009) with a slightly higher degree of detail and without comparison to photometric redshifts.

The results of this exercise (from different inspectors at different epochs done for various purposes) are compressed into a single decision: the inspector agrees or disagrees with the redshift proposed by the pipeline. Table 5 presents the results of the inspections as a function of the redshift quality flags. The higher the flag value, the higher the agreement rate, thus the flags are a good estimator of the redshift quality.

Based on Table 5 one can create a criterion to select the largest number of redshifts for a maximum tolerable error rate. For the purpose of clustering analysis, we use the following criterion to select galaxies with a reliable redshift in the range $0.7 < z < 1.1$ that are brighter than $g < 22.8$ (using DES or CFHT photometry) :

$$\mathrm{zQ} \geq 2 \text{ or } (\mathrm{zQ} \geq 1 \text{ and } \mathrm{zCont} > 0) \text{ or } (\mathrm{zQ} \geq 0 \text{ and } \mathrm{zCont} \geq 2.5). \quad (2)$$

In total, we have inspected the spectra of 2660 galaxies with $0.7 < z < 1.1$ and $g < 22.8$. The criterion excludes 278 objects and keeps 2382 objects. Among the 2382, the inspection disagrees with 22 redshifts, which corresponds to a 1% share. Among the 278 excluded objects, the inspection agrees with 147 redshifts, which is a 52% share. Future pipeline improvement could therefore lead to a maximum improvement of 5.5% in efficiency. For a clustering analysis, we could not simply consider all the redshifts provided by the pipeline as it produces a fraction of incorrect redshifts of about 6%; we need to discard lower-quality redshifts to obtain a more pure sample. With current observations, we cannot determine the impact of such bad redshift exclusion on the redshift distribution and on the clustering measurement.

Table 4. Redshift flags. Low and high SNR correspond to $3 < SNR < 5$ and $5 < SNR$, respectively. We make a special case of the [OII] 3727, 3729 emission line doublet, which is sometimes observed as a blended doublet, sometimes only as single line. The CLASS = 'STAR' category means that the best fit of the pipeline is based on a stellar template.

zQ	meaning
-2	$Z\_ERR > 0.005(1+Z)$ or ZWARNING> 4
-1	CLASS = 'STAR'
1.	one line at low SNR
1.5	two line at low SNR
2.	one line at high SNR
2.5	three or more lines at low SNR
3.	one line at high SNR and at least one line at low SNR
3.5	[OII] 3728 at high SNR
4.	two lines at high SNR
4.5	three or more lines at high SNR
0	none of the conditions above are met
zCont	**meaning**
2.5	magnitude u or g or i or $z < 19.5$
2.	" < 20
1.5	" < 20.5
1	>3 lines with the continuum detected at SNR 10
0.5	>3 " SNR 8

Table 5. Classification of 13,450 visually-inspected redshifts per category of redshift flag. The percentages do not depend on magnitude or selection.

Flags		Inspection result		
zQ	zCont	N	N_{agree}	%
-2.0	0.0	573	71	12.39
-2.0	0.5	13	4	30.77
-2.0	1.0	68	12	17.65
-1.0	0.0	62	6	9.68
-1.0	0.5	7	2	28.57
-1.0	1.0	397	193	48.61
-1.0	2.5	29	28	96.55
0.0	0.0	1453	490	33.72
0.0	0.5	43	23	53.49
0.0	1.0	115	70	60.87
0.0	1.5	76	70	92.11
0.0	2.0	22	18	81.82
0.0	2.5	12	12	100.00
1.0	0.0	618	337	54.53
1.0	0.5	62	55	88.71
1.0	1.0	177	160	90.40
1.0	1.5	61	60	98.36
1.0	2.0	27	26	96.30
1.0	2.5	16	16	100.00
1.5	0.0	274	187	68.25
1.5	0.5	64	53	82.81
1.5	1.0	146	137	93.84
1.5	1.5	36	36	100.00
1.5	2.0	18	18	100.00
1.5	2.5	7	7	100.00
2.0	0.0	218	175	80.28
2.0	0.5	6	2	33.33
2.0	1.0	10	7	70.00
2.0	1.5	26	26	100.00
2.0	2.0	12	12	100.00
2.0	2.5	3	2	66.67
2.5	0.0	136	118	86.76
2.5	0.5	31	30	96.77
2.5	1.0	64	58	90.62
2.5	1.5	27	27	100.00
2.5	2.0	16	16	100.00
2.5	2.5	2	2	100.00
3.0	0.0	205	175	85.37
3.0	0.5	22	20	90.91
3.0	1.0	63	61	96.83
3.0	1.5	46	46	100.00
3.0	2.0	24	23	95.83
3.0	2.5	10	9	90.0
3.5	0.0	1567	1516	96.75
3.5	0.5	335	332	99.10
3.5	1.0	612	612	100.00
3.5	1.5	272	271	99.63
3.5	2.0	126	126	100.00
3.5	2.5	28	28	100.00
4.0	0.0	721	721	100.00
4.0	0.5	251	251	100.00
4.0	1.0	560	560	100.00
4.0	1.5	264	264	100.00
4.0	2.0	99	99	100.00
4.0	2.5	29	29	100.00
4.5	0.0	1036	1036	100.00
4.5	0.5	406	406	100.00
4.5	1.0	1263	1263	100.00
4.5	1.5	398	398	100.00
4.5	2.0	132	132	100.00
4.5	2.5	54	54	100.00

Table 6. Result of the inspection of two plates from eboss 6. The last column is the rate of identification of the spectral class by the inspectors.

name	N	[galaxy / quasar]	star	low SNR	id rate [%]
gri-Uri	858	603 [589 / 14]	17	238	70.28
des bright	635	530 [523 / 07]	0	105	83.46
des faint	658	530 [512 / 18]	1	127	80.55

3.1.1. A more precise classification of plates 8123, 8130

A more thorough redshift inspection to classify the observed spectra by type was performed on two plates belonging to eboss6; see Table 6. The selection algorithms gri-Uri, des bright and des faint target mostly galaxies. Also, the contamination by quasars or stars is small. The main contamination is due to spectra with a low SNR where the redshift cannot be securely determined; they are probably faint galaxies. The current automated classification that identifies the type of object (star, galaxy or quasar) is reliable only for high SNR spectra and not for the low SNR spectra where the class assignmentsshould be trusted.

3.1.2. Comparison with VIPERS redshifts

In the eBOSS ELG test plates, 383 have a match in VIPERS DR1 field W1. We find 370 (97.6%) redshifts in agreement (with $dz/(1+z) \leq 0.005$) and 13 redshifts in disagreement (with $dz/(1+z) > 0.005$). Ten out of the 13 galaxies have a low quality flag in VIPERS and a high quality flag in eBOSS. A second visual inspection of those 13 eBOSS redshifts indicates that they are correct. Three out of 13 have a low quality flag in both VIPERS and eBOSS: both redshift can be doubted. The last category is $3/383 = 0.78\%$ of the total.

3.1.3. Redshift efficiency and fiber number

As shown in Fig. 9 of Bolton et al. (2012), the redshift efficiency decreases for the fiber numbers around 0, 500 and 1000 because they are the most off-center with respect to the spectrograph camera optics. The ELGs demonstrate the same trends.

3.2. Possible line confusions

If there is no continuum detection (zCont= 0), the redshift classes zQ= 1, 2 and 3.5 have a redshift relying on the detection of a single emission line (SEL). The BOSS spectrograph covers 3,600Å to 10,400Å, the prominent lines that can have similar strengths are

- Hα (λ6564) detectable at $z < z^{\rm max}_{\rm H\alpha} = 0.584$,
- [OIII] (λ5007) detectable at $z < z^{\rm max}_{\rm [O_{III}]} = 1.077$,
- Hβ (λ4862) detectable at $z < z^{\rm max}_{\rm [H\beta]} = 1.139$,
- [OII] ($\lambda\lambda$3727,3729) detectable at $z < z^{\rm max}_{\rm [O_{II}]} = 1.790$,

At redshift 1.8, the Lyman α line is at $\lambda = 3,400$Å and cannot be detected. The eBOSS survey will observe first quasar targets with a similar limiting magnitude as ELGs. The quasar sampling is quite complete in particular for bright Lyman alpha quasars (Myers et al. 2015, Palanque-delabrouille et al. 2015). The remaining quasars contamination of the ELG sample will be very small (< 0.5%) and cannot be quantified with current data. We therefore examine the following possible confusions:

$$\lambda^{\rm detection}_{\rm line} = (1+{\rm z_{H\alpha}})\lambda_{\rm H\alpha} = (1+{\rm z_{H\beta}})\lambda_{\rm H\beta} = (1+{\rm z_{[O_{III}]}})\lambda_{\rm [O_{III}]} = (1+{\rm z_{[O_{II}]}})\lambda_{\rm [O_{II}]} \quad (3)$$

We set aside the case zQ=3.5 and zCont=0 as the [OII] doublet is sometimes seen as a blended doublet and therefore provides more information than a single line detection.

The set of observed SEL redshifts as a function of the emission line and SNR is detailed in Table 7. At SNR≥ 5, all SEL redshifts are primarily based on prominent lines (6 exceptions out of 3,329), whereas for the $3 \leq SNR < 5$ SEL redshifts, we encounter a variety of line detections (284 exceptions out of 855).

We re-inspected the low and high SNR line detections that are not in the set of prominent lines: these lines are fitted on residuals of the sky subtraction. The low and high SNR line detections that are found to be prominent lines are not convincing either and line confusion is possible. For this reason, we exclude the classes (zQ=1 or 2) and zCont=0 from the pool of reliable redshifts, in the reliable redshift selection criterion.

There are 3,225 SNR5 [OII] detection cases with zQ=3.5 and zCont=0. For the [OII] line, we fit the share of the flux in each component:

$$\alpha = {\rm flux}_{\lambda 3729}/({\rm flux}_{\lambda 3727} + {\rm flux}_{\lambda 3729}). \quad (4)$$

We define $X = \alpha/\alpha_{err}$ and show a few [OII] lines measurements and fits that span the range of X values. We find that X is correlated to the SNR detection of the line; see Fig 3. On average, if the doublet is detected at SNR 7, then the double Gaussian model is significantly more accurate than a simple Gaussian model. Note that, at redshift 0.8, the typical velocity dispersion in the ELG is around 70 km s^{-1}, so that in the fits, the line width of each component is dominated by the instrumental resolution (Comparat et al. 2013a).

Table 7. Repartition of the SEL redshifts, 3329 with SNR5 and 855 with SNR3, in the complete BOSS/eBOSS ELG sample and in the fiducial eBOSS target selections decam 190 and decam 240, see Section 4 for their definition.

line	N	decam 190	decam 240
$3 \leq SNR < 5$ (zQ=1 and zCont=0)			
[Ar_{III}] (λ 7137)	8	0	0
Hϵ (λ 3970)	33	0	0
Hδ (λ 4102)	17	0	0
Hγ (λ 4341)	34	2	2
Hβ (λ 4862)	12	0	0
Hα (λ 6564)	39	0	0
He_{II} (λ 4686)	14	1	1
He_{II} (λ 5411)	8	0	0
[N_{II}] (λ 6549)	6	0	0
[N_{II}] (λ 6585)	19	0	0
[Ne_{III}] (λ 3869)	47	0	0
[O_{II}] (λ 6302)	17	1	1
[O_{II}] (λ 6365)	6	0	0
[O_{II}] (λ 3728)	488	16	18
[O_{III}] (λ 4363)	27	0	0
[O_{III}] (λ 4960)	17	0	0
[O_{III}] (λ 5007)	44	1	1
[S_{II}] (λ 6718)	10	1	1
[S_{II}] (λ 6732)	9	0	0
SNR≥5 ((zQ=2 or 3.5) and zCont=0)			
Hγ (λ 4341)	1	0	0
Hβ (λ 4862)	1	0	0
Hα (λ 6564)	85	0	1
[N_{II}] (λ 6585)	2	0	1
[Ne_{III}] (λ 3869)	2	0	0
[O_{II}] (λ 3728)	3225	268	354
[O_{III}] (λ 5007)	13	1	1

3.3. Pipeline redshift error

The previous subsection demonstrated that the redshift failures are correlated with the SNR in the lines. We now quantify this statement using the pipeline redshift errors.

We consider all the redshifts (with zQ≥ -1) and the correlation between the detection SNR of the line, the redshift and redshift error. Fig. 4 shows the redshift error as a function of redshift coded with the emission line SNR for the lines Hα Hβ, [OII] and [OIII] 5007. Whatever the redshift, the SNR of the line SNR is highly anti-correlated with the redshift error: the higher the SNR, the lower the error. The impact of the sky brightness on the redshift error is also evident: for a fixed SNR in a line, the redshift error increases and decreases as the sky brightness. A SNR=3 in the [OII] line corresponds to an average error of $z_{err} \sim (1+z) \times 10^{-4}$, suggesting that the pipeline redshift errors are within the requirements. To conclude, the stronger the emission lines, the more accurate the centroid of the redshift.

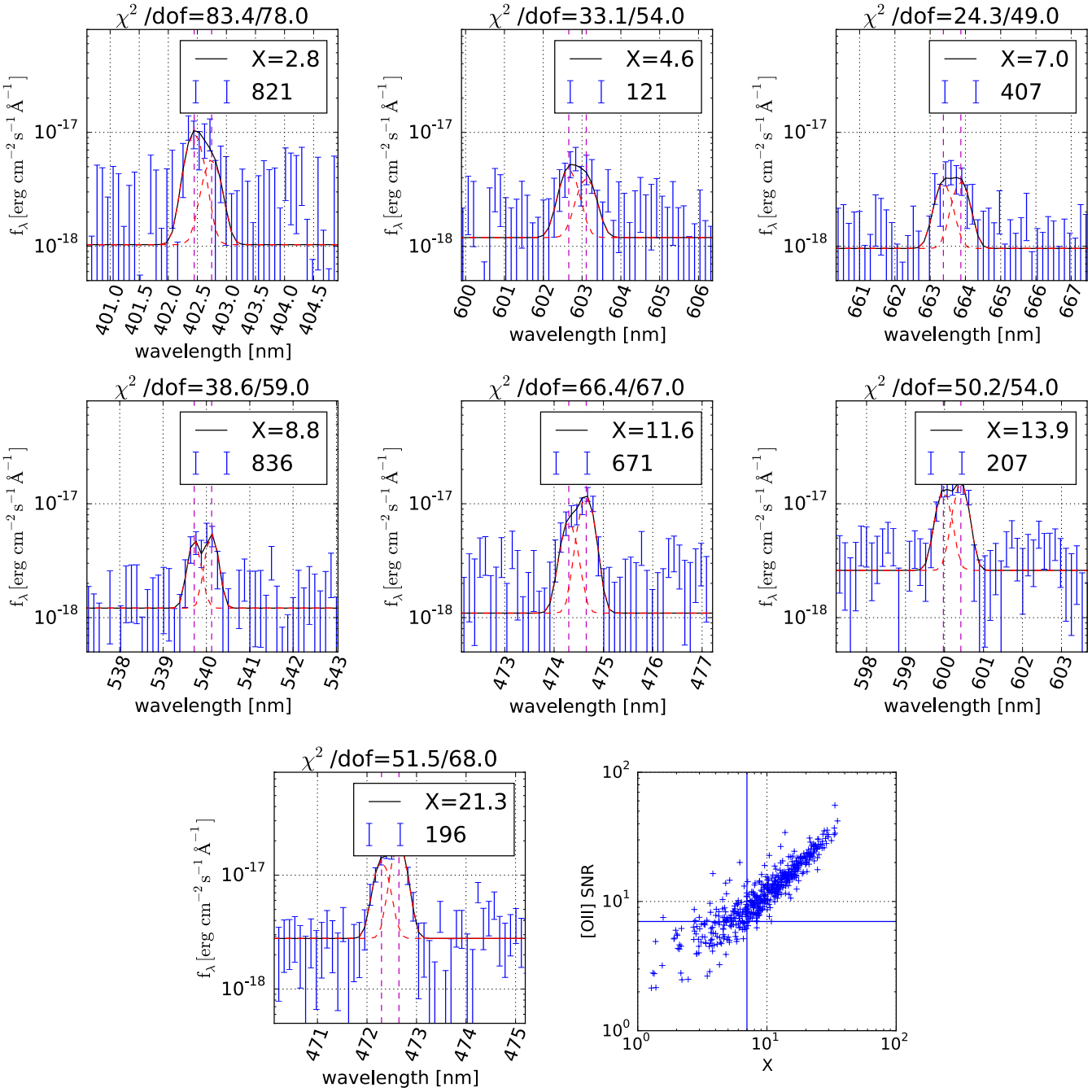

Fig. 3. Example of fits of the [OII] doublets by a double Gaussian on some spectra from plate 8130. Each spectrum (blue error bars) is designated by its fiber number and the fits (black solid) are characterized by the χ^2/dof given above each panel. We show the two individual Gaussians in red dashes. The vertical magenta dashed lines are at $(1+z)\lambda_{[OII]}$. The panels are ordered by increasing value of X. Around a value of X=7, the blended doublet start to be a better model than a single gaussian. The last panel shows the [OII] SNR vs. X with horizontal and vertical solid lines at a value of 7.

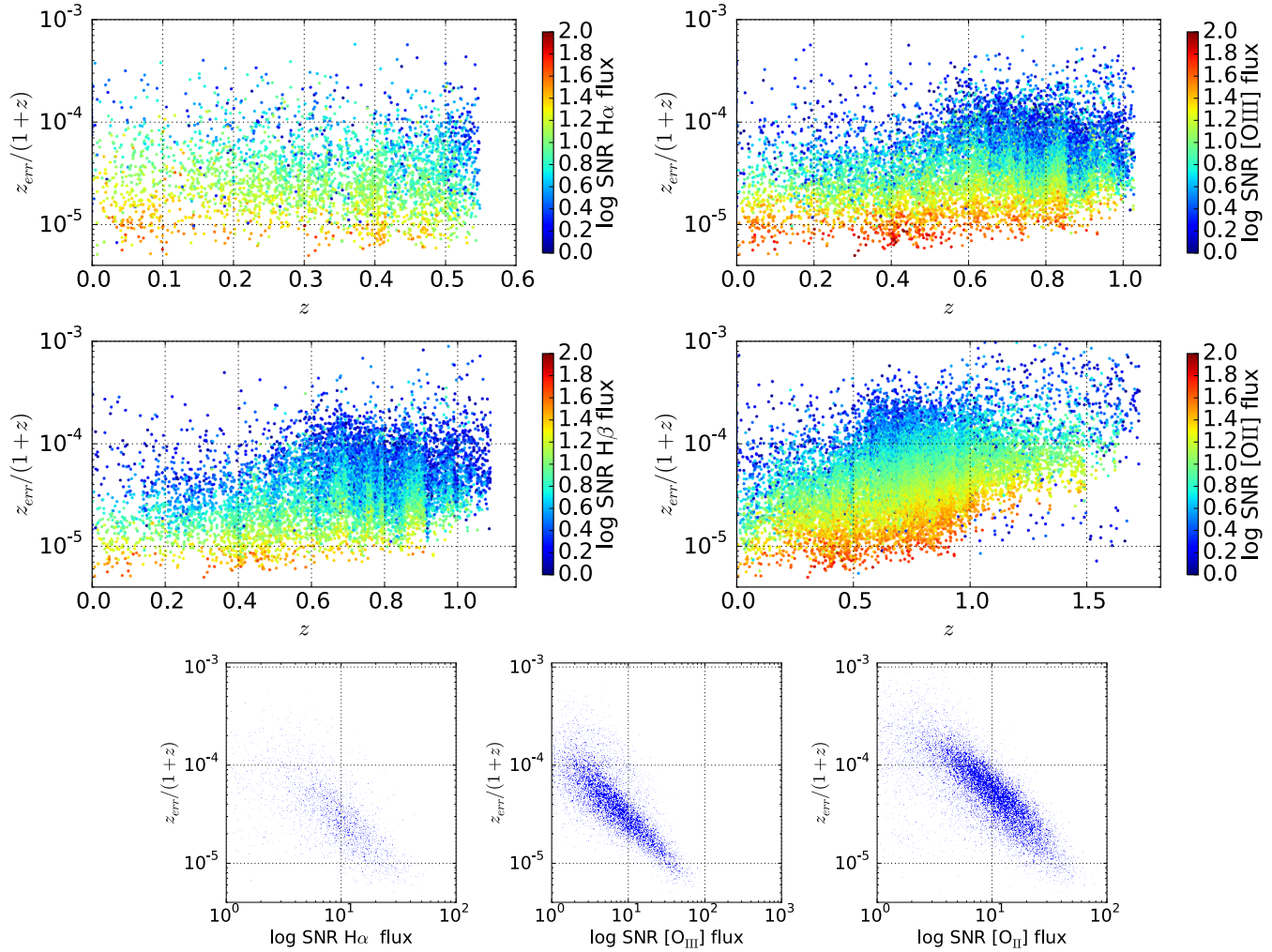

Fig. 4. Redshift uncertainty vs redshift for the ELGs for the Hα , [OIII] , Hβ and [OII] emission lines detected coded as a function of the log of the detection SNR. We see the imprint of the sky emission line in the variation of SNR with redshift. The last row presents the correlation between redshift error and line SNR detection. The redshift error is anti-correlated with the line SNR.

4. Target selection for eBOSS using DECam imaging

Using the eboss6 and 7 observations, we can further optimize the DECam-based target selection to increase its efficiency for the purpose of eBOSS ELG selection. The further optimization of the Fisher algorithms is presented in Raichoor et al. (2015).

The requirement to determine the BAO standard ruler with a 2% precision at redshift $\sim 0.8 - 0.9$ can be met with 255,000 fibers producing 190,000 accurate redshifts in the range $0.7 < z < 1.1$ observed on an area between 500 (V=0.5 h^{-3} Gpc^3, density $\rho = 1.3 \times 10^{-3} h^3$ Mpc^{-3}) and 1500 deg^2 (V=1.5 h^{-3} Gpc^3, density $\rho = 4.2 \times 10^{-4} h^3$ Mpc^{-3}); see Dawson et al. (2015) for a detailed discussion of the survey strategy. Therefore the 'efficiency' of the TS algorithm must reach:

$$f_{obs}^{ELG}(0.7 < z_{reliable} < 1.1)/N_{targets}^{ELG} > 190/255 = 74.5\%. \quad (5)$$

Additionally, the fraction of catastrophic redshifts in the range $0.7 < z < 1.1$ must be below 1%.

To define the efficiency, we specify the selection done on the redshift flag into two categories: good and bad redshifts. We trust redshifts that fall in the category (zQ≥ 2 or [zQ≥ 1 and zCont> 0] or [zQ≥ 0 and zCont≥ 2.5]) and consider the other redshifts as not reliable. Based on this assumption, we can define redshift distributions and tune color selections. The redshift distributions in the data section are obtained using this criterion as well.

Here, we present two further optimizations of DECam-based ELG TS algorithms, that both reach the requirements. Both selections have the same bright star contamination exclusion scheme. We keep detections with $g_{2"} - g_{\rm model} < 2$ and $r_{2"} - r_{\rm model} < 2$ and $z_{2"} - z_{\rm model} < 2$.

The first algorithm, designated 'decam 190', selects 190.4±3.7 targets per deg^2 and outputs $N(0.7 < z_{good} < 1.1) = 78.2 \pm 1.1\%$ with a mean redshift at 0.855. The redshift identification rate is 91±0.6%. The selections are:

1. $21.6 < g_{\rm model} < 22.8$
2. $0.3 < g_{\rm model} - r_{\rm model} < 0.7$ and $0.25 < r_{\rm model} - z_{\rm model} < 1.4$
3. $0.45(g_{\rm model} - r_{\rm model}) + 0.4 < r_{\rm model} - z_{\rm model} > 0.7(g_{\rm model} - r_{\rm model}) + 0.8$

The second algorithm, designated 'decam 240', selects 241.3±4.2 targets per deg^2. It has $N(0.7 < z_{good} < 1.1) = 74.5 \pm 0.5\%$ with a mean redshift at 0.871. The identification rate is 90±0.5%. The selections are:

1. $21.5 < g_{\rm model} < 22.8$
2. $0.2 < g_{\rm model} - r_{\rm model} < 0.7$ and $0.25 < r_{\rm model} - z_{\rm model} < 1.4$
3. $0.45(g_{\rm model} - r_{\rm model}) + 0.4 < r_{\rm model} - z_{\rm model} < 0.8(g_{\rm model} - r_{\rm model}) + 1$

These numbers are based on the observation of 1,553 (decam 240) and 1,246 (decam 190) targets in eboss6 and eboss7. The redshift distributions of both selections are given in Tables 8, A.4. The decam 190 has a narrower redshift range than decam 240 and targets slightly lower redshift galaxies. Figure 5 shows the selection boxes in the $g - r$, $r - z$ plane. An independent study of these selection on the COSMOS [OII] catalog (Comparat et al. 2015) and its corresponding DECam photometry[1] provides the same redshift distributions and success rates.

The two selection schemes presented here were chosen among a handful of other selections producing similar efficiencies and densities. To do so, we sorted all possible selection schemes with the mean [OII] emission line flux so that those two schemes guarantee strong lines.

SEL redshifts

For the proposed decam 190 and decam 240 selections less than 0.5% of the targets fall in the category SEL.

Bias

Using the current spectroscopic data (eboss 6-7) and applying the same methodology described in Jouvel et al. (2015), we can measure the monopole clustering and deduce the galaxy bias for both samples: $b = 1.7 \pm 0.1$. The further optimization of the selection in the redshift range 0.7 to 1.1 increased the efficiency without changing the clustering amplitude.

[1] http://legacysurvey.org/

Table 8. Cumulative redshift distribution of the optimized DES selections.

algorithm	Q10	Q25	Q50	Q75	Q90
decam 190	0.736	0.787	0.855	0.927	1.071
decam 240	0.741	0.794	0.871	0.961	1.142

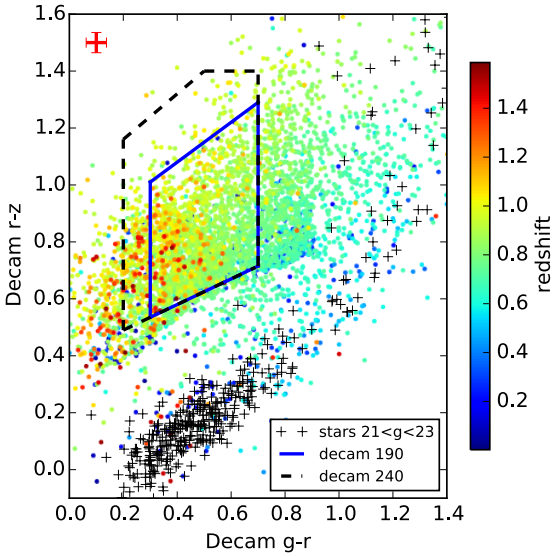

Fig. 5. Color-color diagram showing the optimized DECam-based ELG selection algorithms. We show all the good spectroscopic redshifts observed by eboss6 and 7. Two boundaries are common to both selections. The decam 240 selection box is more extended towards bluer and higher redshift galaxies. The mean error on the DES colors is shown with the red cross in the top-left corner.

5. Summary

In this article, we:

- documented the eBOSS ELG pilot survey: 9,000 new spectra targeted from different photometric surveys. We provide robust redshift distributions for each selection scheme;
- demonstrated that the automated redshift estimation is robust, in particular, the possible line confusion rate is confined to sub-percent level;
- further optimized and finalized one of the possible eBOSS ELG selection using DECam-based imaging. The obtained selection can reach a density between 190 and 240 ELG deg^{-2} for a galaxy bias of 1.7±0.1 and an efficiency between 74 and 78 percent.
- We find that the selection decam 190 is best-suited for a wide angle survey to measure precisely the BAO in the two-point correlation function at redshift 0.85.

Future plans

It appears that the ELG samples under construction will be extremely useful to investigate the galaxy population that forms stars the most efficiently.

The spectroscopic signature of ELGs is quite specific and mixes light emitted by the stellar population (which is a combination of recently formed stars and older ones and light reprocessed by the interstellar medium) and by the circumgalactic medium. To grasp a global panchromatic view of these galaxies, we will study in the future the infra-red light emitted by their dust component.

By combining *N*-body simulations with semi-analytical models that reproduce observations, we expect push further the analysis from Favole et al. (2015) in order to provide a more complete description of the properties of ELGs, clarify their nature and maximize their potential for constraining cosmological models.

Acknowledgements

JC and FP acknowledge support from the Spanish MICINNs Consolider-Ingenio 2010 Programme under grant MultiDark CSD2009-00064, MINECO Centro de Excelencia Severo Ochoa Programme under the grants SEV-2012-0249, FPA2012-34694, and the projects AYA2014-60641-C2-1-P and AYA2012-31101. We also thank the Lawrence Berkeley National Laboratory for its hospitality. FP acknowledges the spanish MEC "Salvador de Madariaga" program, Ref. PRX14/00444. TD and JPK acknowledge support from the LIDA ERC advanced grant. AR acknowledges funding from the P2IO LabEx (ANR-10-LABX-0038) in the framework "Investissements d'Avenir" (ANR- 11-IDEX-0003-01) managed by the French National Research Agency (ANR). EJ acknowledges the support of CNRS and the Labex OCEVU.

This paper represents an effort by the SDSS-III, SDSS-IV and DES collaborations.

Funding for SDSS-III was provided by the Alfred P. Sloan Foundation, the Participating Institutions, the National Science Foundation, and the U.S. Department of Energy Office of Science. The SDSS web site is www.sdss.org.

SDSS-IV acknowledges support and resources from the Center for High-Performance Computing at the University of Utah.

SDSS-IV is managed by the Astrophysical Research Consortium for the Participating Institutions of the SDSS Collaboration including the Brazilian Participation Group, the Carnegie Institution for Science, Carnegie Mellon University, the Chilean Participation Group, the French Participation Group, Harvard-Smithsonian Center for Astrophysics, Instituto de Astrofísica de Canarias, The Johns Hopkins University, Kavli Institute for the Physics and Mathematics of the Universe (IPMU) / University of Tokyo, Lawrence Berkeley National Laboratory, Leibniz Institut für Astrophysik Potsdam (AIP), Max-Planck-Institut für Astronomie (MPIA Heidelberg), Max-Planck-Institut für Astrophysik (MPA Garching), Max-Planck-Institut für Extraterrestrische Physik (MPE), National Astronomical Observatory of China, New Mexico State University, New York University, University of Notre Dame, Observatário Nacional / MCTI, The Ohio State University, Pennsylvania State University, Shanghai Astronomical Observatory, United Kingdom Participation Group, Universidad Nacional Autónoma de México, University of Arizona, University of Colorado Boulder, University of Portsmouth, University of Utah, University of Virginia, University of Washington, University of Wisconsin, Vanderbilt University, Yale University and the french participation group.

Funding for the DES Projects has been provided by the U.S. Department of Energy, the U.S. National Science Foundation, the Ministry of Science and Education of Spain, the Science and Technology Facilities Council of the United Kingdom, the Higher Education Funding Council for England, the National Center for Supercomputing Applications at the University of Illinois at Urbana-Champaign, the Kavli Institute of Cosmological Physics at the University of Chicago, the Center for Cosmology and Astro-Particle Physics at the Ohio State University, the Mitchell Institute for Fundamental Physics and Astronomy at Texas A&M University, Financiadora de Estudos e Projetos, Fundação Carlos Chagas Filho de Amparo à Pesquisa do Estado do Rio de Janeiro, Conselho Nacional de Desenvolvimento Científico e Tecnológico and the Ministério da Ciência, Tecnologia e Inovação, the Deutsche Forschungsgemeinschaft and the Collaborating Institutions in the Dark Energy Survey.

The Collaborating Institutions are Argonne National Laboratory, the University of California at Santa Cruz, the University of Cambridge, Centro de Investigaciones Energéticas, Medioambientales y Tecnológicas-Madrid, the University of Chicago, University College London, the DES-Brazil Consortium, the University of Edinburgh, the Eidgenössische Technische Hochschule (ETH) Zürich, Fermi National Accelerator Laboratory, the University of Illinois at Urbana-Champaign, the Institut de Ciències de l'Espai (IEEC/CSIC), the Institut de Física d'Altes Energies, Lawrence Berkeley National Laboratory, the Ludwig-Maximilians Universität München and the associated Excellence Cluster Universe, the University of Michigan, the National Optical Astronomy Observatory, the University of Nottingham, The Ohio State University, the University of Pennsylvania, the University of Portsmouth, SLAC National Accelerator Laboratory, Stanford University, the University of Sussex, and Texas A&M University.

The DES data management system is supported by the National Science Foundation under Grant Number AST-1138766. The DES participants from Spanish institutions are partially supported by MINECO under grants AYA2012-39559, ESP2013-48274, FPA2013-47986, and Centro de Excelencia Severo Ochoa SEV-2012-0234. Research leading to these results has received funding from the European Research Council under the European Union's Seventh Framework Programme (FP7/2007-2013) including ERC grant agreements 240672, 291329, and 306478.

We are grateful for the extraordinary contributions of our CTIO colleagues and the DECam Construction, Commissioning and Science Verification teams in achieving the excellent instrument and telescope conditions that have made this work possible. The success of this project also relies critically on the expertise and dedication of the DES Data Management group.

This paper includes targets derived from the images of the Wide-Field Infrared Survey Explorer, which is a joint project of the University of California, Los Angeles, and the Jet Propulsion Laboratory/California Institute of Technology, funded by the National Aeronautics and Space Administration.

This paper has gone through internal review by the DES collaboration.

References

Ahn, C. P., Alexandroff, R., Allende Prieto, C., et al. 2012, ApJS, 203, 21
Alam, S., Albareti, F. D., Allende Prieto, C., et al. 2015, ArXiv e-prints [arXiv:1501.00963]
Anderson, L., Aubourg, É., Bailey, S., et al. 2014, MNRAS, 441, 24
Banerji, M., Jouvel, S., Lin, H., et al. 2015, MNRAS, 446, 2523
Ben Zhu, G., Comparat, J., Kneib, J.-P., et al. 2015, ArXiv e-prints [arXiv:1507.07979]
Bolton, A. S., Schlegel, D. J., Aubourg, É., et al. 2012, AJ, 144, 144
Boulade, O., Charlot, X., Abbon, P., et al. 2003, in Society of Photo-Optical Instrumentation Engineers (SPIE) Conference Series, Vol. 4841, Instrument Design and Performance for Optical/Infrared Ground-based Telescopes, ed. M. Iye & A. F. M. Moorwood, 72–81
Bovy, J., Myers, A. D., Hennawi, J. F., et al. 2012, ApJ, 749, 41
Comparat, J., Kneib, J.-P., Bacon, R., et al. 2013a, A&A, 559, A18
Comparat, J., Kneib, J.-P., Escoffier, S., et al. 2013b, MNRAS, 428, 1498
Comparat, J., Richard, J., Kneib, J.-P., et al. 2015, A&A, 575, A40
Dawson, K. S., Kneib, J.-P., Percival, W. J., et al. 2015, ArXiv e-prints [arXiv:1508.04473]
Dawson, K. S., Schlegel, D. J., Ahn, C. P., et al. 2013, AJ, 145, 10
de la Torre, S., Guzzo, L., Peacock, J. A., et al. 2013, A&A, 557, A54
Delubac, T., Bautista, J. E., Busca, N. G., et al. 2015, A&A, 574, A59
Diehl, H. T., Abbott, T. M. C., Annis, J., et al. 2014, in Society of Photo-Optical Instrumentation Engineers (SPIE) Conference Series, Vol. 9149, Society of Photo-Optical Instrumentation Engineers (SPIE) Conference Series, 0V
Doel, P., Brooks, D., Antonik, M. L., et al. 2012, in Society of Photo-Optical Instrumentation Engineers (SPIE) Conference Series, Vol. 8446, Society of Photo-Optical Instrumentation Engineers (SPIE) Conference Series, 6F
Drinkwater, M. J., Jurek, R. J., Blake, C., et al. 2010, MNRAS, 401, 1429
Eisenstein, D. J., Weinberg, D. H., Agol, E., et al. 2011, AJ, 142, 72
Favole, G., Comparat, J., Prada, F., et al. 2015, ArXiv e-prints [arXiv:1507.04356]
Fisher, R. A. 1936, Annals of Eugenics, 7, 179
Flaugher, B. 2012, in APS April Meeting Abstracts, D7007
Flaugher, B. & Bebek, C. 2014, in Society of Photo-Optical Instrumentation Engineers (SPIE) Conference Series, Vol. 9147, Society of Photo-Optical Instrumentation Engineers (SPIE) Conference Series, 0S

Flaugher, B. & DES Collaboration. 2013, in American Astronomical Society Meeting Abstracts, Vol. 221, American Astronomical Society Meeting Abstracts #221, #335.02

Flaugher, B., Diehl, H. T., Honscheid, K., et al. 2015, ArXiv e-prints [arXiv:1504.02900]

Fukugita, M., Ichikawa, T., Gunn, J. E., et al. 1996, AJ, 111, 1748

Garilli, B., Guzzo, L., Scodeggio, M., et al. 2014, A&A, 562, A23

Gunn, J. E., Carr, M., Rockosi, C., et al. 1998, AJ, 116, 3040

Gunn, J. E., Siegmund, W. A., Mannery, E. J., et al. 2006, AJ, 131, 2332

Guzzo, L., Scodeggio, M., Garilli, B., et al. 2014, A&A, 566, A108

Gwyn, S. D. J. 2012, AJ, 143, 38

Kazin, E. A., Koda, J., Blake, C., et al. 2014, MNRAS, 441, 3524

Lang, D., Hogg, D. W., & Schlegel, D. J. 2014, ArXiv e-prints [arXiv:1410.7397]

Le Fèvre, O., Cassata, P., Cucciati, O., et al. 2013, A&A, 559, A14

Le Fèvre, O., Saisse, M., Mancini, D., et al. 2003, in Society of Photo-Optical Instrumentation Engineers (SPIE) Conference Series, Vol. 4841, Instrument Design and Performance for Optical/Infrared Ground-based Telescopes, ed. M. Iye & A. F. M. Moorwood, 1670–1681

Lilly, S. J., Le Brun, V., Maier, C., et al. 2009, ApJS, 184, 218

Maraston, C., Pforr, J., Henriques, B. M., et al. 2013, MNRAS, 435, 2764

Martinez, V. & Saar, E. 2002, in Society of Photo-Optical Instrumentation Engineers (SPIE) Conference Series, Vol. 4847, Astronomical Data Analysis II, ed. J.-L. Starck & F. D. Murtagh, 86–100

Myers, A. D., Palanque-Delabrouille, N., Prakash, A., et al. 2015, ArXiv e-prints [arXiv:1508.04472]

Newman, J. A., Cooper, M. C., Davis, M., et al. 2013, ApJS, 208, 5

Oke, J. B. & Gunn, J. E. 1983, ApJ, 266, 713

Prakash, A., Licquia, T. C., Newman, J. A., et al. 2015, ArXiv e-prints [arXiv:1508.04478]

Raichoor, A., Comparat, J., Delubac, T., et al. 2015, ArXiv e-prints [arXiv:1505.01797]

Schlegel, D. J., Finkbeiner, D. P., & Davis, M. 1998, ApJ, 500, 525

Schneider, D. P., Richards, G. T., Hall, P. B., et al. 2010, AJ, 139, 2360

Seo, H.-J. & Eisenstein, D. J. 2003, ApJ, 598, 720

Sharp, R., Saunders, W., Smith, G., et al. 2006, in Society of Photo-Optical Instrumentation Engineers (SPIE) Conference Series, Vol. 6269, Society of Photo-Optical Instrumentation Engineers (SPIE) Conference Series, 0G

Shen, Y., Brandt, W. N., Dawson, K. S., et al. 2015, ApJS, 216, 4

Smee, S. A., Gunn, J. E., Uomoto, A., et al. 2013, AJ, 146, 32

Weinberg, D. H., Mortonson, M. J., Eisenstein, D. J., et al. 2013, Phys. Rep., 530, 87

Wright, E. L., Eisenhardt, P. R. M., Mainzer, A. K., et al. 2010, AJ, 140, 1868

Zou, H., Jiang, Z., Zhou, X., et al. 2015, The Astronomical Journal, 150, 104

[1] Instituto de Fisica Teorica UAM/CSIC, Universidad Autónoma de Madrid, Cantoblanco, E-28049 Madrid, Spain

[2] Departamento de Fisica Teorica, Universidad Autónoma de Madrid, Cantoblanco, E-28049 Madrid, Spain

[3] Laboratoire d'Astrophysique, Ecole Polytechnique Fédérale de Lausanne (EPFL), Observatoire de Sauverny, CH-1290 Versoix, Switzerland

[4] Department of Physics and Astronomy, University College London, Gower Street, London WC1E6BT, UK

[5] CEA, Centre de Saclay, IRFU/SPP, F-91191 Gif-sur-Yvette, France

[6] Aix Marseille Université, CNRS, LAM (Laboratoire d'Astrophysique de Marseille) UMR 7326, F-13388, Marseille, France

[7] Department of Physics & Electronics, Rhodes University, Grahamstown 6140, South Africa

[8] Institute of Cosmology and Gravitation, University of Portsmouth, Portsmouth, PO1 3FX, UK

[9] Department of Physics & Astronomy, Johns Hopkins University, 3400 N. Charles Street, Baltimore, MD 21218, USA

[10] Instituto de Astrofísica de Andalucía (CSIC), Glorieta de la Astronomía, E-18080 Granada, Spain

[11] Lawrence Berkeley National Laboratory, 1 Cyclotron Road, Berkeley, CA, 94720, USA

[12] Key Laboratory of Optical Astronomy, National Astronomical Observatories, Chinese Academy of Sciences, Beijing, 100012,China

[13] Department of Physics and Astronomy, University of Utah, 115 S 1400 E, Salt Lake City, UT 84112, USA

[14] Apache Point Observatory and New Mexico State University, P.O. Box 59, Sunspot, NM, 88349-0059, USA

[15] Sternberg Astronomical Institute, Moscow State University, Moscow

[16] CPPM, Aix-Marseille Université, CNRS/IN2P3, Marseille, France

[17] Department of Physics and Astronomy and PITT PACC, University of Pittsburgh, Pittsburgh, PA 15260, USA

[18] Department of Astronomy and Astrophysics, The Pennsylvania State University, University Park, PA 16802

[19] Institute for Gravitation and the Cosmos, The Pennsylvania State University, University Park, PA 16802

[20] Cerro Tololo Inter-American Observatory, National Optical Astronomy Observatory, Casilla 603, La Serena, Chile

[21] Fermi National Accelerator Laboratory, P. O. Box 500, Batavia, IL 60510, USA

[22] Institute of Astronomy, University of Cambridge, Madingley Road, Cambridge CB3 0HA, UK

[23] Kavli Institute for Cosmology, University of Cambridge, Madingley Road, Cambridge CB3 0HA, UK

[24] CNRS, UMR 7095, Institut d'Astrophysique de Paris, F-75014, Paris, France

[25] Sorbonne Universités, UPMC Univ Paris 06, UMR 7095, Institut d'Astrophysique de Paris, F-75014, Paris, France

[26] Laboratório Interinstitucional de e-Astronomia - LIneA, Rua Gal. José Cristino 77, Rio de Janeiro, RJ - 20921-400, Brazil

[27] Observatório Nacional, Rua Gal. José Cristino 77, Rio de Janeiro, RJ - 20921-400, Brazil

[28] Department of Astronomy, University of Illinois, 1002 W. Green Street, Urbana, IL 61801, USA

[29] National Center for Supercomputing Applications, 1205 West Clark St., Urbana, IL 61801, USA

[30] Institut de Ciències de l'Espai, IEEC-CSIC, Campus UAB, Carrer de Can Magrans, s/n, 08193 Bellaterra, Barcelona, Spain

[31] Institut de Física d'Altes Energies, Universitat Autònoma de Barcelona, E-08193 Bellaterra, Barcelona, Spain

[32] Kavli Institute for Particle Astrophysics & Cosmology, P. O. Box 2450, Stanford University, Stanford, CA 94305, USA

[33] Excellence Cluster Universe, Boltzmannstr. 2, 85748 Garching, Germany

[34] Faculty of Physics, Ludwig-Maximilians University, Scheinerstr. 1, 81679 Munich, Germany

[35] Department of Physics and Astronomy, University of Pennsylvania, Philadelphia, PA 19104, USA

[36] Jet Propulsion Laboratory, California Institute of Technology, 4800 Oak Grove Dr., Pasadena, CA 91109, USA

[37] Kavli Institute for Cosmological Physics, University of Chicago, Chicago, IL 60637, USA

[38] Department of Physics, University of Michigan, Ann Arbor, MI 48109, USA

[39] Max Planck Institute for Extraterrestrial Physics, Giessenbachstrasse, 85748 Garching, Germany

Appendix A: Redshift distributions

Table A.1. Redshift distribution for reliably identified redshifts per square degree during eboss6 observations N= $N_{obs}(z_{min} < z \leq z_{max})/TSR$/area. The error given is taken from a Poisson distribution: $\sigma_N = N/\sqrt{N_{obs}}$. The area is of 13.36 deg^2.

redshift		gri-Uri	
z_{min}	z_{max}	N [deg^{-2}]	σ_N
0.0	0.1	2.06	0.40
0.1	0.2	2.62	0.46
0.2	0.3	3.49	0.53
0.3	0.4	3.96	0.56
0.4	0.5	4.68	0.61
0.5	0.6	9.12	0.85
0.6	0.7	26.64	1.45
0.7	0.8	41.39	1.81
0.8	0.9	24.97	1.41
0.9	1.0	10.47	0.91
1.0	1.1	2.46	0.44
1.1	1.2	0.40	0.18
1.2	1.3	0.24	0.14
1.3	1.4	0.48	0.19
1.4	1.5	0.24	0.14
1.5	1.6	0.16	0.11
1.6	2.4	0.71	0.24
total		134.07	3.25
ID rate		0.68	

Table A.2. Same as Table A.1 for the Fisher selections observed by eboss6 or eboss7 on the eboss7 footprint: the area is of 8.82 deg^2.

redshift		UgrizW		UgrizW bright		UgrizW bright all		griW	
z_{min}	z_{max}	N	σ_N	N	σ_N	N	σ_N	N	σ_N
0.0	0.1	2.94	0.59	0.74	0.30	3.56	0.65	1.90	0.47
0.1	0.2	2.00	0.48	0.61	0.27	2.49	0.54	2.38	0.53
0.2	0.3	2.47	0.54	0.36	0.21	2.71	0.57	3.21	0.62
0.3	0.4	2.58	0.55	0.25	0.17	2.48	0.54	2.62	0.56
0.4	0.5	3.17	0.61	1.23	0.39	3.93	0.68	3.80	0.67
0.5	0.6	6.34	0.86	2.45	0.55	7.15	0.92	8.22	0.99
0.6	0.7	19.38	1.51	8.41	1.01	23.21	1.66	29.26	1.87
0.7	0.8	42.29	2.23	8.33	1.01	41.46	2.22	37.60	2.11
0.8	0.9	40.41	2.18	4.41	0.74	36.48	2.08	32.11	1.95
0.9	1.0	16.45	1.39	1.59	0.44	14.63	1.31	10.86	1.13
1.0	1.1	4.23	0.70	0.98	0.35	4.98	0.77	3.06	0.60
1.1	1.2	1.88	0.47	0.12	0.12	1.77	0.46	1.06	0.35
1.2	1.3	1.06	0.35	0.25	0.17	1.30	0.39	0.47	0.24
1.3	1.4	1.29	0.39	0.12	0.12	1.18	0.37	0.71	0.29
1.4	1.5	0.59	0.26	0.37	0.21	0.96	0.34	0.59	0.26
1.5	1.6	1.41	0.41	0.24	0.17	1.42	0.41	0.94	0.33
1.6	2.4	3.88	0.67	0.62	0.28	4.26	0.71	2.95	0.59
total		152.35	4.22	31.09	1.95	153.96	4.27	141.76	4.09
ID rate		0.76		0.71		0.78		0.72	

Table A.3. Same as Table A.1 for the DES selections, based on eboss 6-7 spectra in eboss 7 area that has a higher completeness.

redshift		des-b		des-f	
z_{min}	z_{max}	N	σ_N	N	σ_N
0.0	0.1	1.77	0.51	4.06	0.83
0.1	0.2	8.21	1.14	8.64	1.21
0.2	0.3	12.09	1.39	3.92	0.82
0.3	0.4	11.97	1.38	4.84	0.90
0.4	0.5	3.37	0.70	3.14	0.72
0.5	0.6	7.79	1.08	4.39	0.83
0.6	0.7	32.18	2.19	6.63	1.02
0.7	0.8	106.24	3.95	71.49	3.44
0.8	0.9	112.60	4.05	117.35	4.39
0.9	1.0	73.51	3.32	72.50	3.44
1.0	1.1	33.83	2.29	44.64	2.71
1.1	1.2	17.44	1.65	28.94	2.19
1.2	1.3	13.20	1.44	22.51	1.94
1.3	1.4	6.80	1.04	15.33	1.60
1.4	1.5	7.28	1.07	15.27	1.60
1.5	1.6	1.52	0.48	4.37	0.86
1.6	2.4	18.35	1.69	32.01	2.29
total		468.15	8.34	460.05	8.64
ID rate		0.76		0.71	

Table A.4. Redshift distribution for the algorithm selecting 190 and 240 ELG per deg^2.

redshift		decam 190		decam 240	
z_{min}	z_{max}	N/A [deg^{-2}]	log N/V [h^{-3} Mpc^3]	N/A [deg^{-2}]	log N/V [h^{-3} Mpc^3]
-0.1	0.0	0.0		0.0	
0.0	0.1	0.6	-3.62	0.6	-3.61
0.1	0.2	1.7	-3.98	2.4	-3.83
0.2	0.3	1.6	-4.40	2.0	-4.31
0.3	0.4	1.0	-4.83	1.2	-4.76
0.4	0.5	0.6	-5.23	0.7	-5.15
0.5	0.6	1.2	-5.07	1.7	-4.92
0.6	0.7	3.3	-4.72	3.7	-4.67
0.7	0.8	40.7	-3.71	44.1	-3.67
0.8	0.9	65.3	-3.56	74.1	-3.50
0.9	1.0	30.9	-3.93	43.7	-3.78
1.0	1.1	11.1	-4.42	16.9	-4.23
1.1	1.2	5.1	-4.79	7.7	-4.60
1.2	1.3	3.1	-5.03	5.4	-4.79
1.3	1.4	1.7	-5.30	3.5	-4.99
1.4	1.5	0.8	-5.63	1.8	-5.31
1.5	1.6	0.7	-5.72	0.7	-5.71
1.6	1.7	0.3	-6.04	0.9	-5.64
1.7	1.8	0.3	-6.05	0.7	-5.74
1.8	1.9	0.5	-5.88	0.9	-5.65
1.9	2.0	0.4	-5.97	0.8	-5.71
2.0	2.1	0.3	-6.13	0.8	-5.70
2.1	2.2	0.7	-5.76	0.7	-5.75
2.2	2.3	0.5	-5.88	0.5	-5.87
2.3	2.4	0.0		0.2	-6.37
total [deg^{-2}]		172.72	-	215.8	-
ID rate [%]		0.91	-	0.90	-